

Supplementary Information:

Relationship of roll and pitch oscillations in a fin flapping at transitional to high Reynolds numbers

Authors: Promode R. Bandyopadhyay, David N. Beal, J. Dana Hrubes, and Arun Mangalam

This supplementary information comprises Part 1: Data and Part 2: Video.

Part 1: Data

1.1 Nomenclature:

The fin profiles were measured at different spans to confirm that the fin twisted without the production of any camber, as shown in figure SI1. Therefore, the results are free of cambering effects.

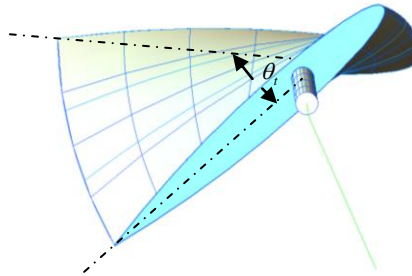


Figure SI1. Schematic of camberless twisting of fin.

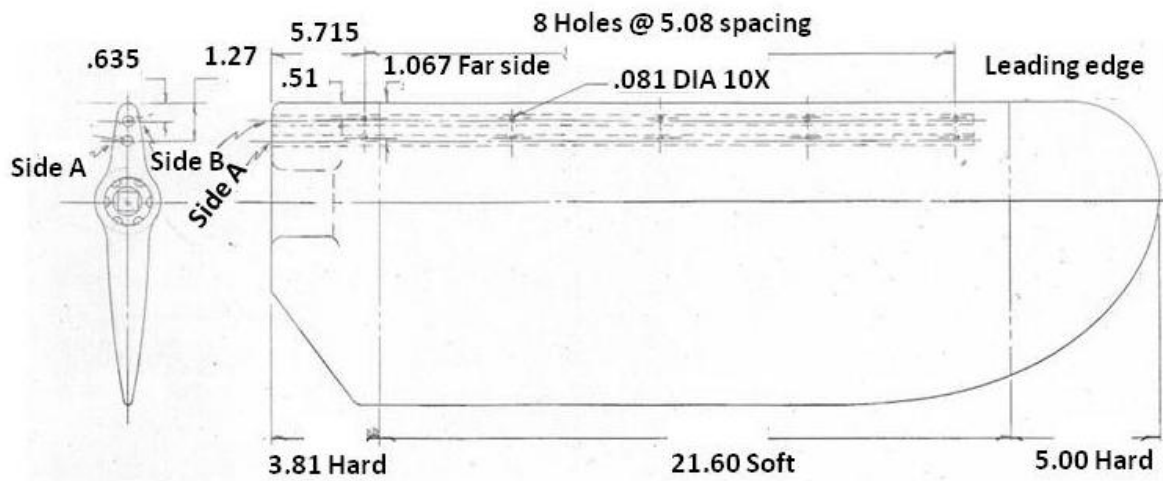
1.2 Dye visualization:

Dot dye: Sigma Aldrich Brilliant Green Dye B-6756 (research grade, not food grade) was used in the early work with non-twisting fins (see figure 5 in paper). Dissolvable dye “buttons” were created, following inspiration from Ellington. On the stove a sucrose solution was created and dye was added until a smooth consistency with a deep color was achieved. This thick paste was immediately applied as “dots” or “buttons” at various locations on the fin and allowed to dry overnight. During flow visualization tests, the dye buttons dissolved in the surrounding water and created visualization trails.

Dye injection: In the later visualizations (figure 9 to 11) comparing the leading-edge vortex in twisting and non-twisting fins during hovering, liquid dye was plumbed through holes on the fin surface. See figure SI2. Figure SI2a shows the dimensions of the flexible fin and the dye port layout. Figure SI2b shows the dye plumbing. Figure SI2c shows a photograph of the dye injection apparatus.

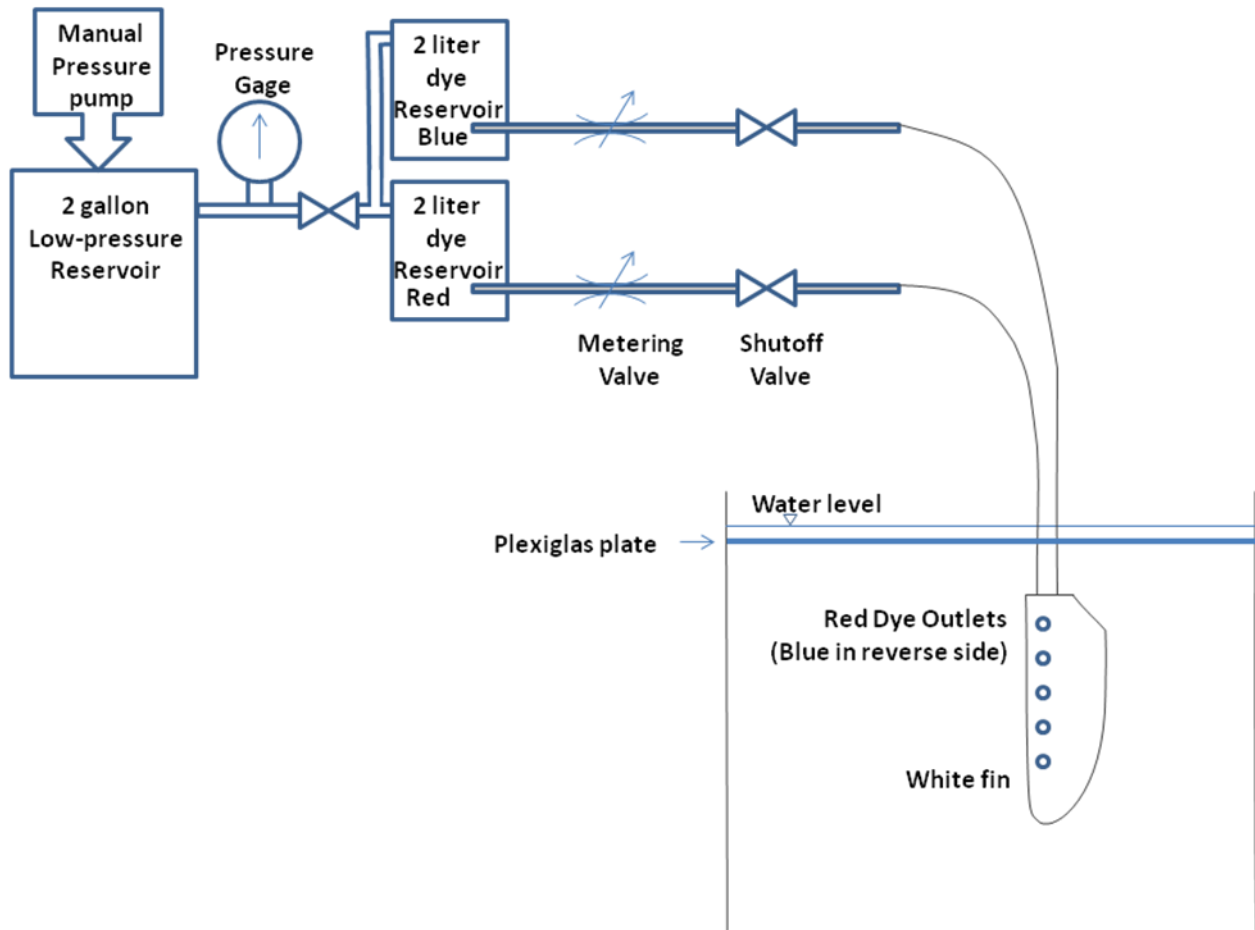
Red and blue dyes were injected slightly under pressure, each on opposing sides of the fin near the leading edge and through five surface-flush ports along the span. The dyes used were Hilton-Davis FD&C Red #40 certified food color and Sigma Aldrich Brilliant Green Dye B-6756. A minimum amount was dissolved in water to produce a vivid visualization image. Whole milk of less than 10% fat content was added to inhibit diffusion of the dye mixture in water.

We had a spray unit with a hand pump that had a capacity of approximately 1 gallon. It is the type of spray bottle used in the yard to spray insecticide. That output was used to simultaneously pressurize two separate bottles that contained the two different color dyes. Each output of the two dye bottles ran through a controlling needle valve which then fed to the foil. A few test runs were made to find the optimum setting for each needle valve resulting in the desired dye flow rate. For each run, the pressure was pumped to a predetermined value while monitoring a pressure gauge and the duration of the run was short to keep the feed pressure and flow rate nearly constant.

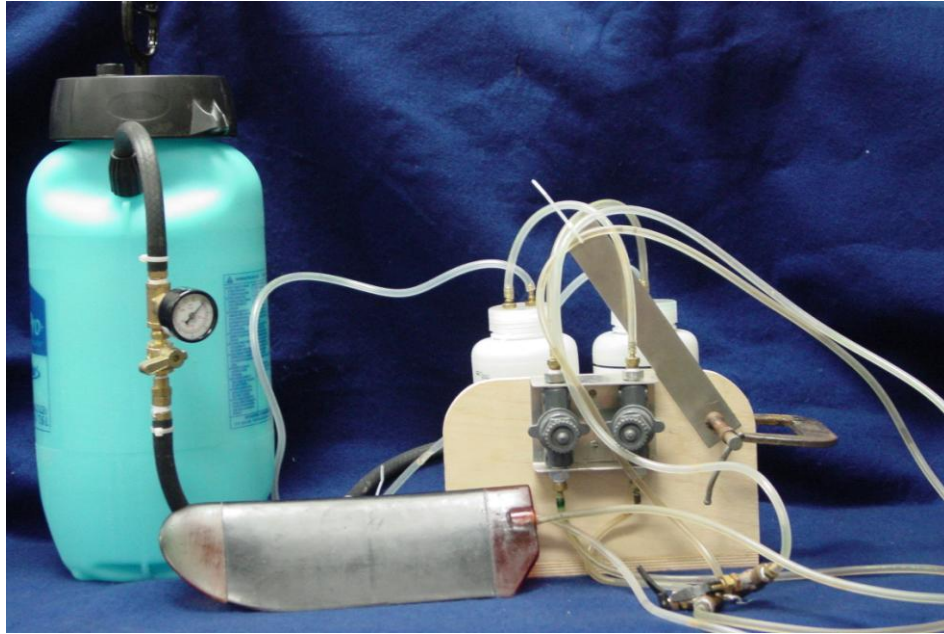


Flex fin with dye ports; Scales Full; Dimensions are in cm

(a)



(b)



(c)

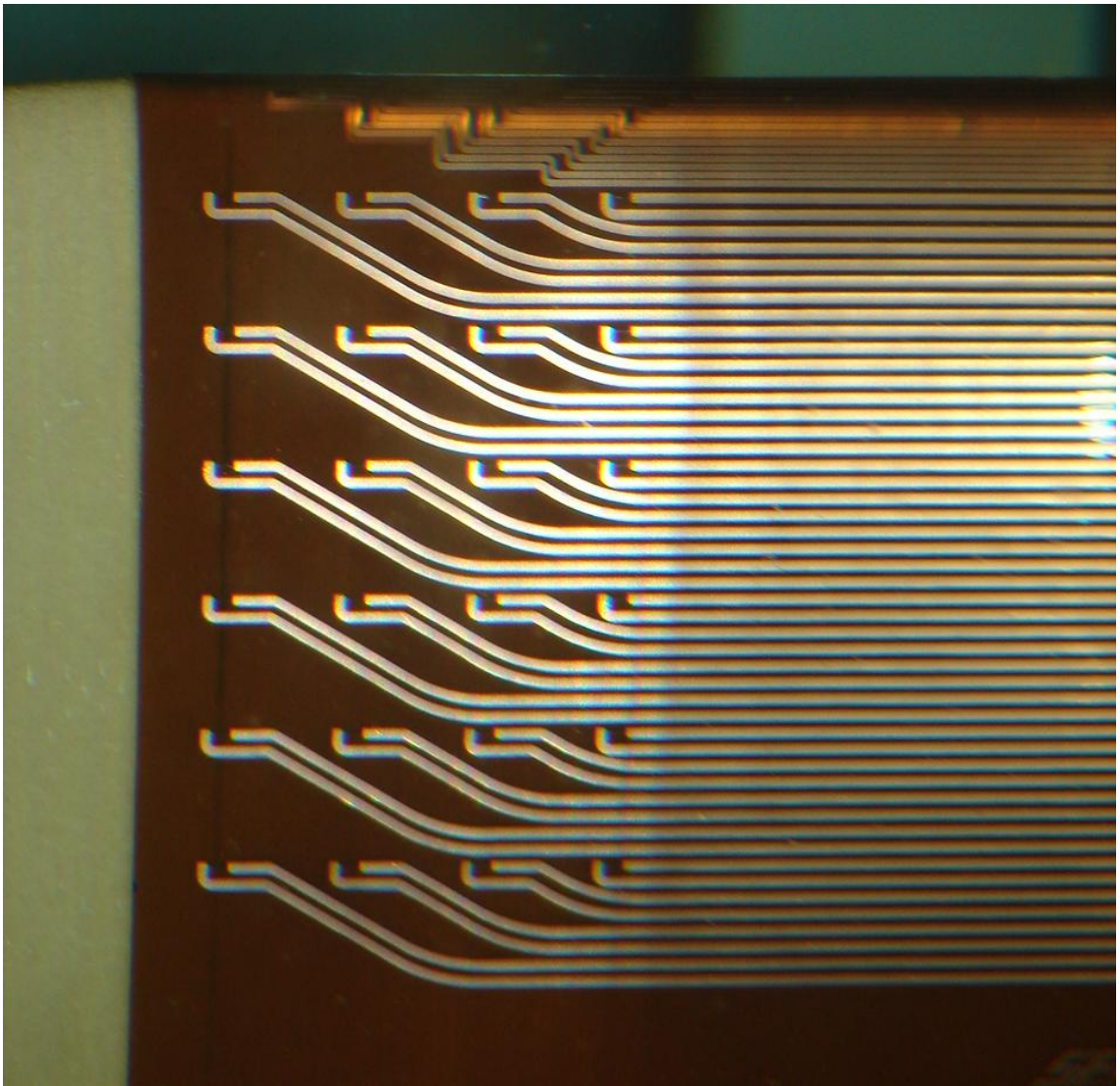
Figure SI2. Layout of the injection holes on the flexible fin (a); the dimensions are in cm. Dye injection plumbing: (b) schematic; (c) photograph.

Camera: We used two Sony Handy-Cam Camcorders and using manual focus control, but we used automatic exposure control so the f-stop is unknown. The lens focal length was unknown, because we just used the zoom lens to frame the desired image. The frame rate was standard 30 frames/second and the resolution was standard 640 by 480 pixels.

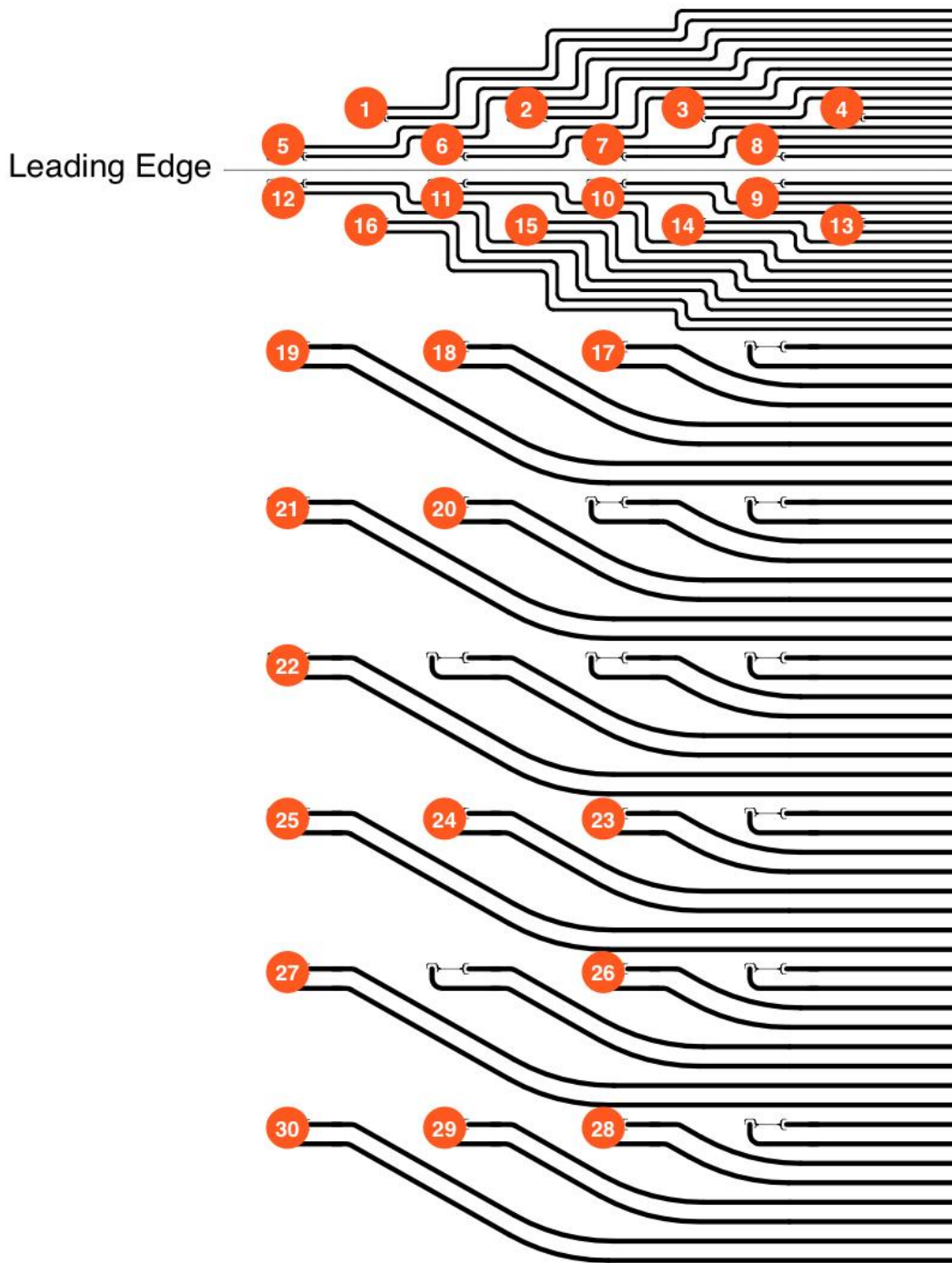
1.3 Wall-shear stress gauge array layout:

Figure SI3a shows a photograph of the rigid fin populated with the surface hot-film array.

Figure SI3b shows the layout of the array. Note that the array is closely spaced near the leading edge.



(a)



(b)

Figure SI3. Layout of the staggered surface hot-film array on the fin. (a) Photograph of the fin (NACA0012-34 section with slightly thickened trailing edge). The chord (10.16 cm) runs vertically, and the span (20.32 cm) runs horizontally. (b) Chordwise and spanwise stagger of the

film locations. The hot-film gauge spacing is narrower near the leading edge. The gauges are denoted by the numbers in the red circles. They are sequenced left to right above the broken line marked “leading edge” and right to left below that. There are inactive gauges in rows 5 – 10, counting from the top.

Static Calibration: Figure SI4 shows the time traces of the ho-film outputs; the vertical axis contains the sensor numbers (S-01, ...). Figure SI4 shows that the data acquisition and signal analysis are capturing the phase reversal at the stagnation point at pitch amplitude of 0° . The point of stagnation lies between sensors 5 and 12 (see figure SI3 above), whose strip-chart voltage recordings are shown in the second and third rows, respectively.

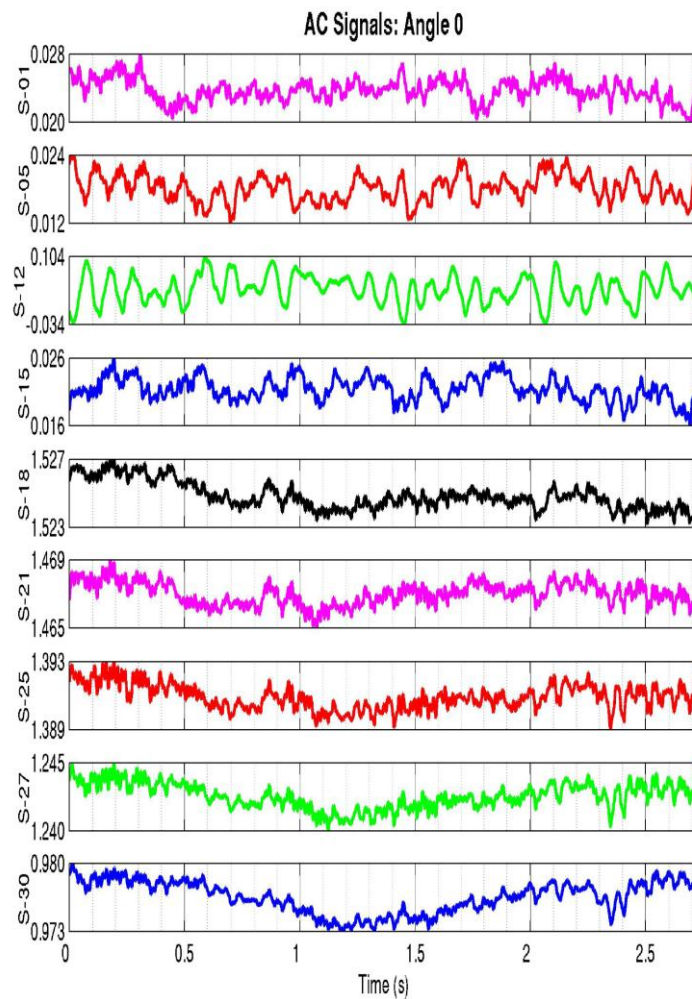
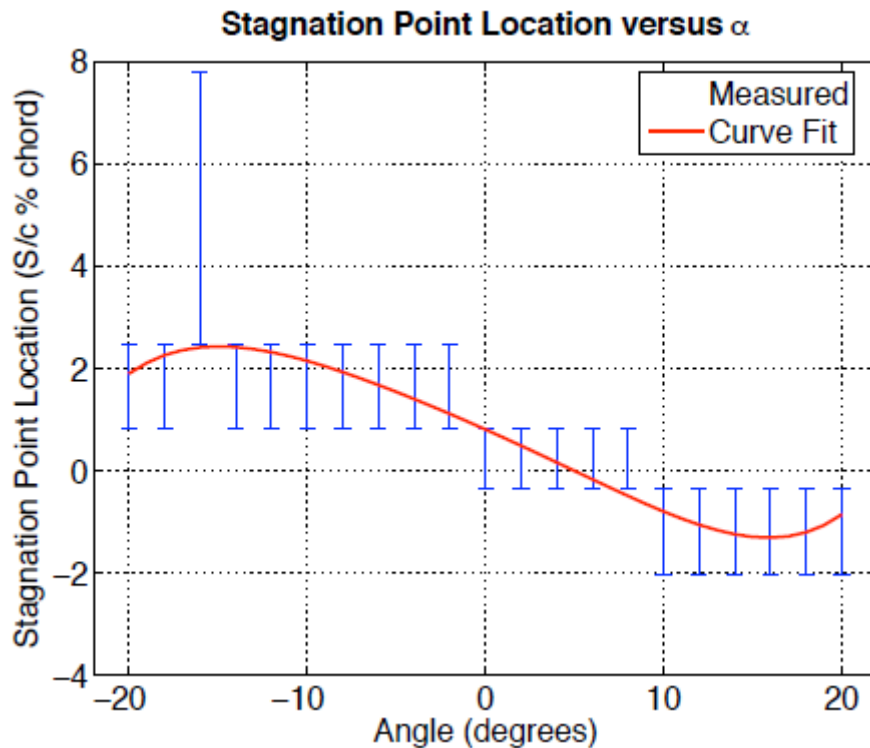
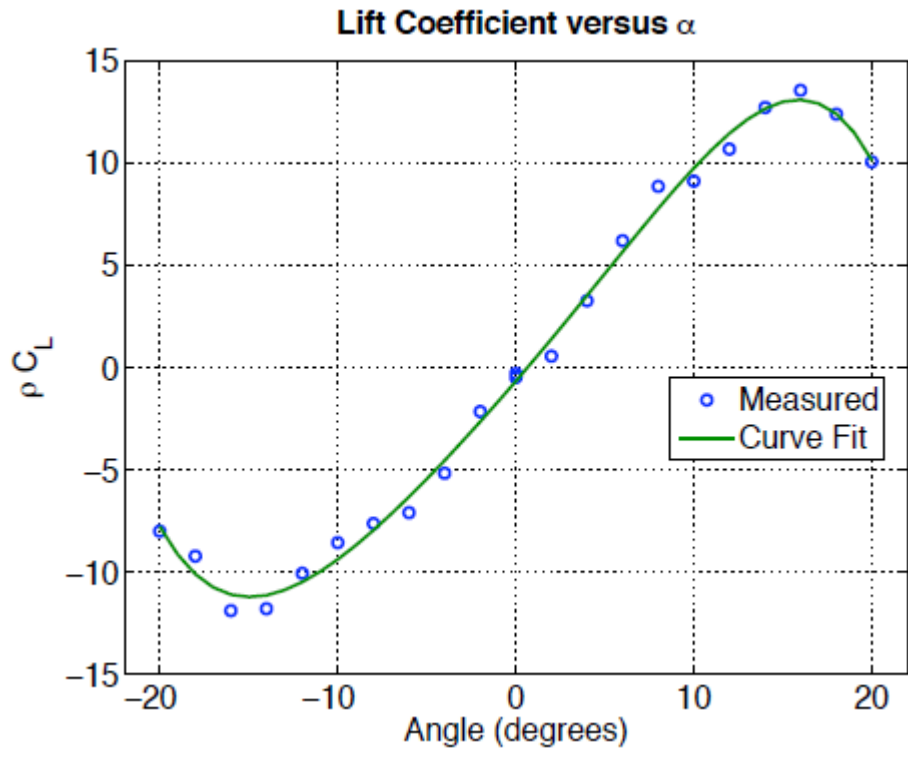


Figure SI4. Phase reversal verification between sensors 5 (S-05) and 12 (S-12) (second and third strip-charts from top); pitch amplitude is zero degrees.

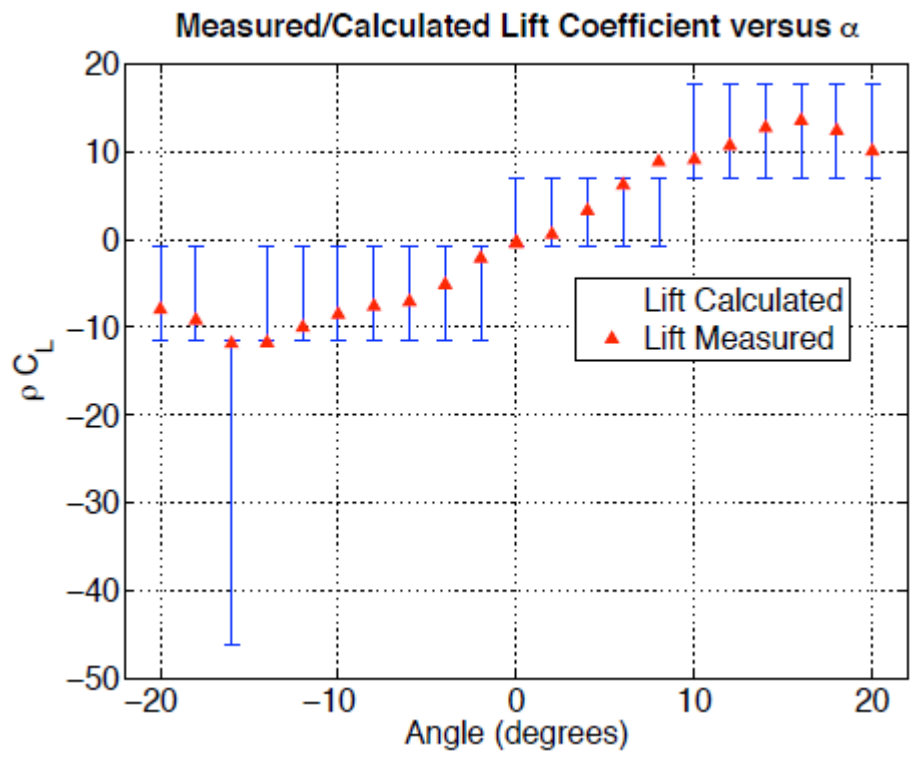
Figure SI5 shows the results of data analysis for obtaining the static relationship between the location of the stagnation point and lift. Obtaining all the stagnation point locations over the entire range of pitch angles (-20° to 20° in 2° increments) produces figure SI5 (a). The stagnation point location in figure SI5 (a) is essentially a range between two sensor locations determined through the phase reversal, as shown in figure SI4. The curve-fit in lift is a fifth-order polynomial fit.



(a) Stagnation point location.



(b) Distribution of lift coefficient.



(c) Comparison of measured and calculated lift. The equation in section 2.2 of the paper (equation 13 in the paper) is a fit to the data as shown above.

Figure SI5. Static relationship between the location of the stagnation point and lift.

1.4. Relationship between St , pitch amplitude, angle of attack at the average span, thrust and efficiency:

Measurements of efficiency and thrust are shown in Figures SI6 to SI9. In Figures SI6 and SI7, the axes are Strouhal number versus pitch amplitude, and in figures SI8 and SI9, the axes are Strouhal number versus angle of attack at the average radial location of the fin span. Figures SI6 and SI8 show efficiency and figures SI7 and SI9 show thrust.

In figure SI6, note that efficiency reaches the maximum value (> 0.57) in a narrow region of Strouhal number and pitch amplitude (shown by the solid line). Figure SI7 shows the direction where thrust drops. Figure SI8 marks the region where efficiency is > 0.57 . Figure SI9 marks the region where efficiency is maximum (> 0.57). Figures SI8 and 9 also show the region where thrust is a maximum, but efficiency is low.

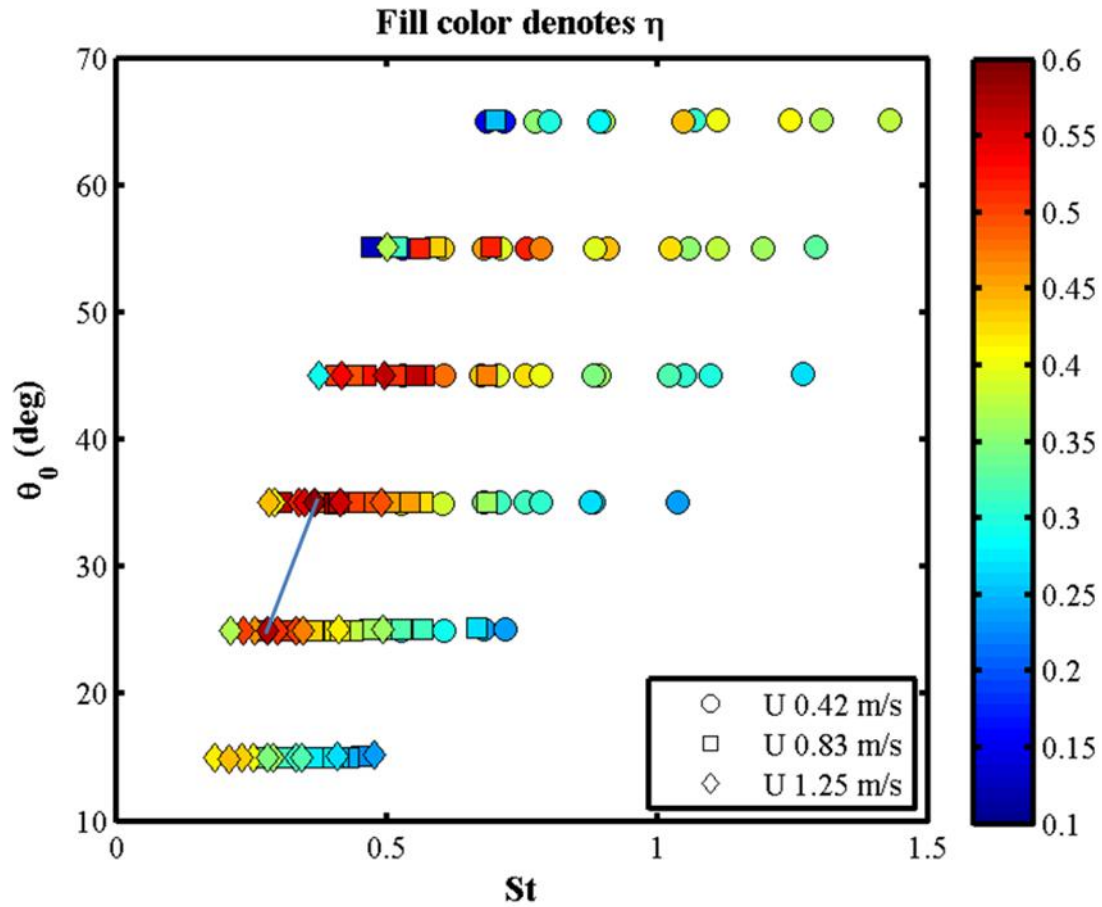


Figure SI6. There are blue regions at both high and low St boundaries. So, there is a ridge in between. This figure shows that for high eta (deep red) you get a steep ridge. We are seeing how resonance is optimizing the flow. Untwisted fin. The blue line shows where efficiency is a maximum. All data are for tow.

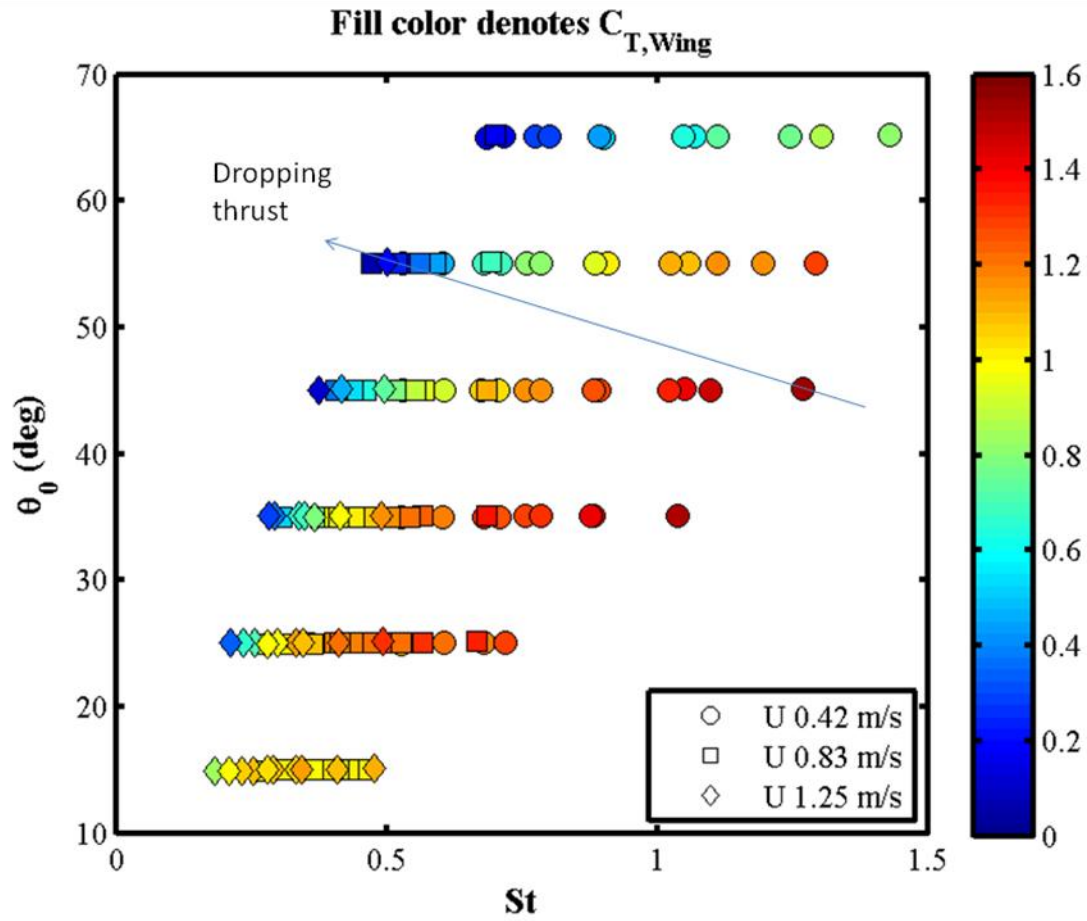


Figure S17. Figure shows when thrust drops. Untwisted fin. All data are for tow.

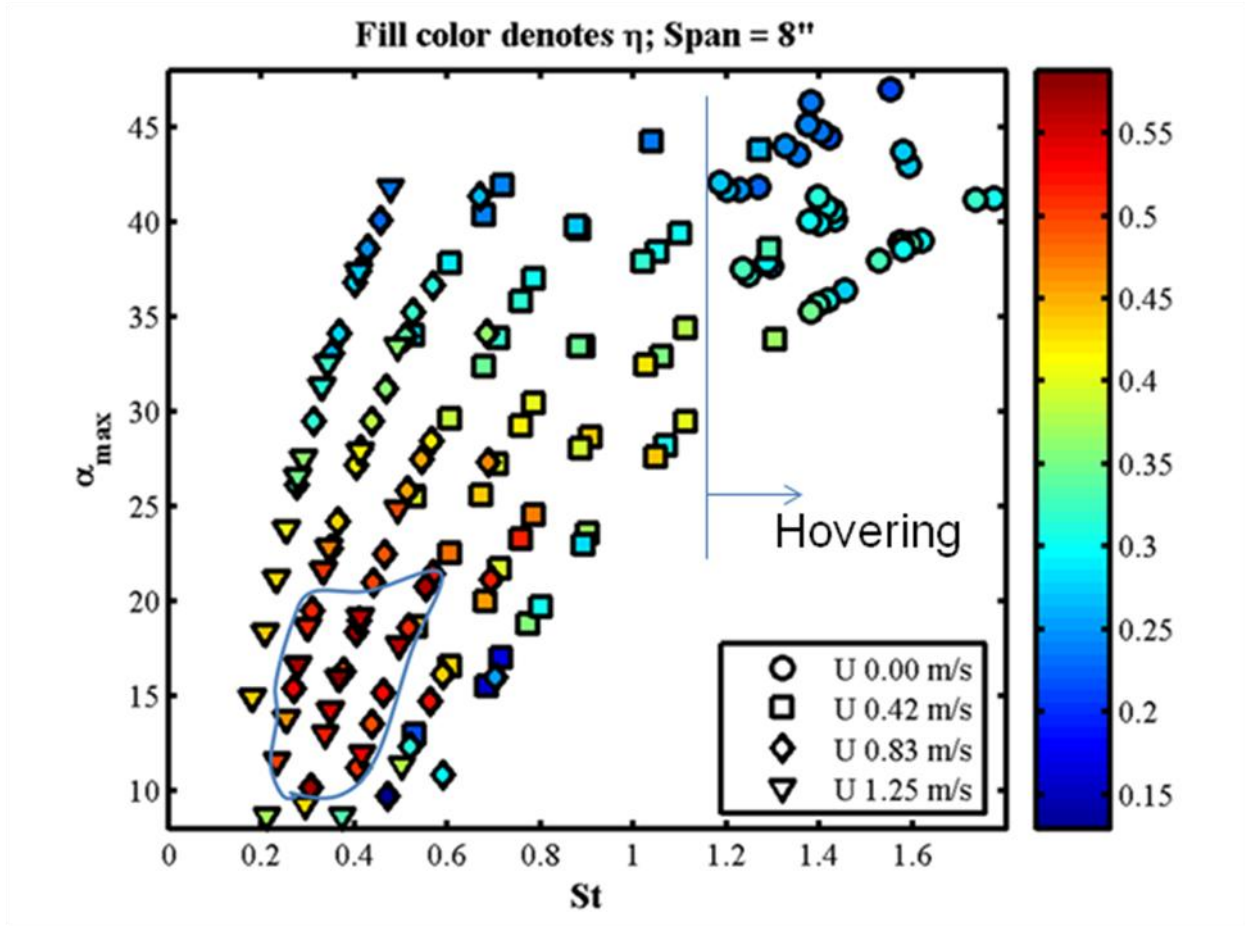


Figure SI8. Efficiency drops rapidly at the St boundaries of the marked high η region. Untwisted fin. Note that St and η during hovering are based on the induced velocity which was modeled assuming disk flow (Wakeling & Ellington 1997). The hovering data follow the trend of the tow data.

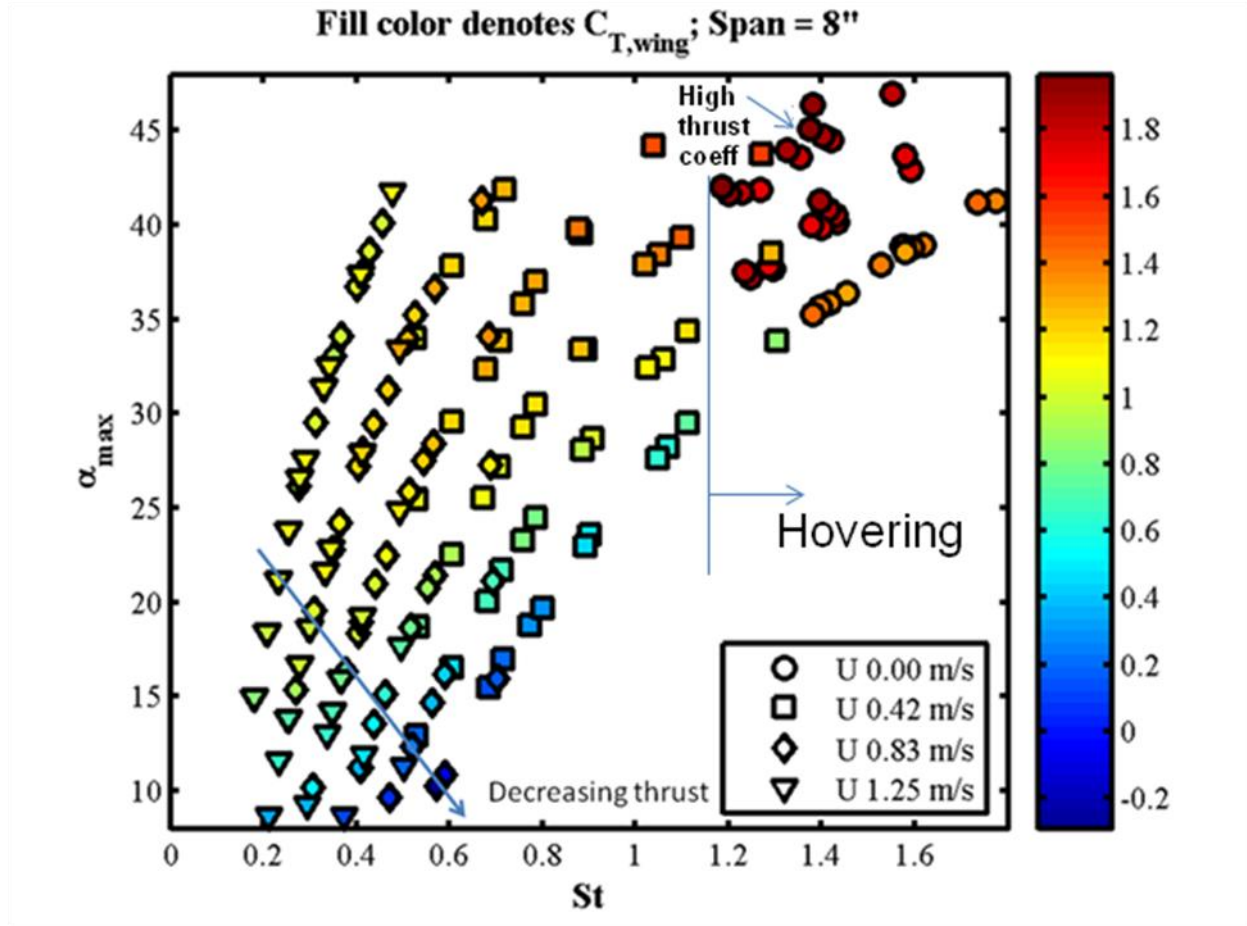
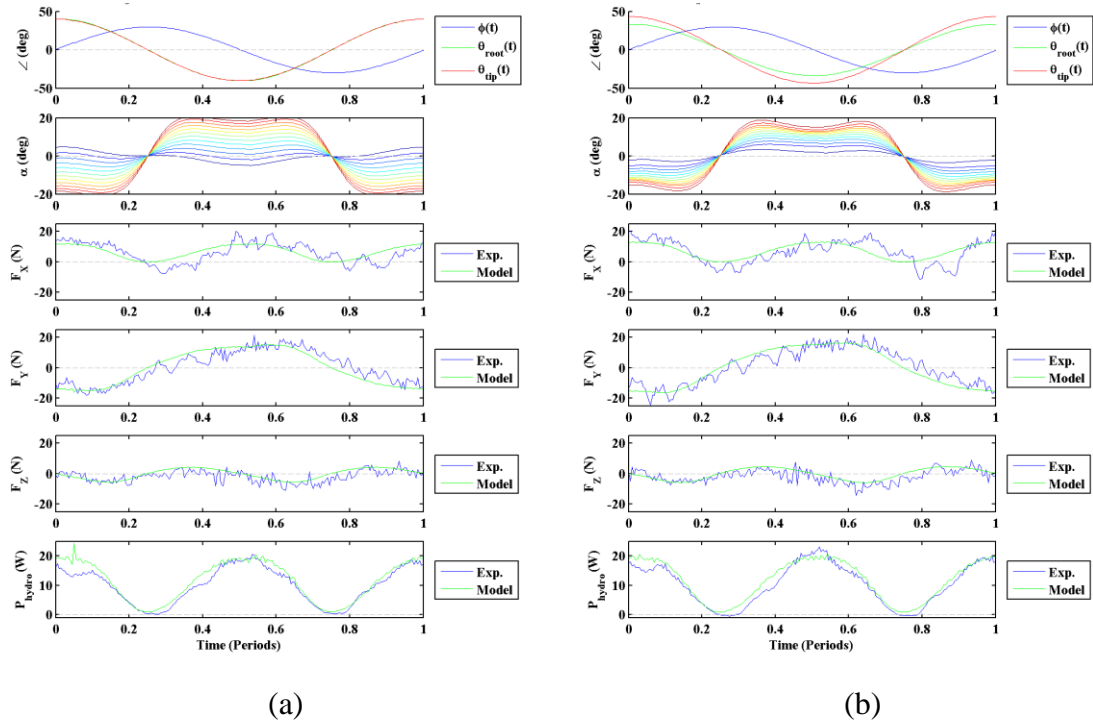
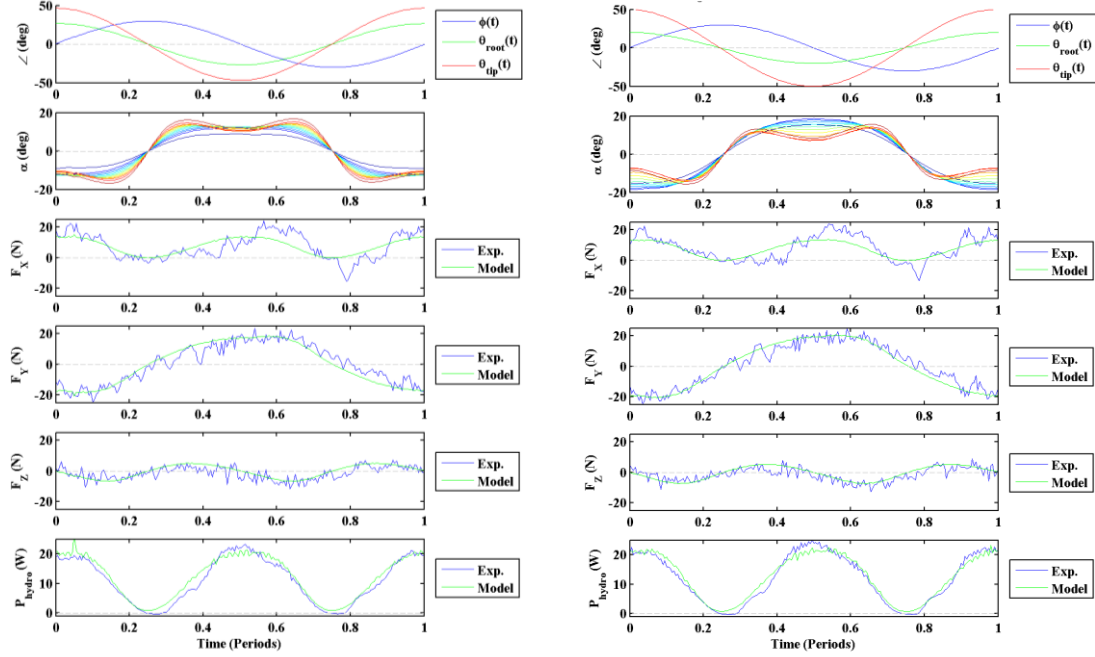


Figure SI9. Figure shows the direction of drop in thrust in the favored St region. Very high thrust is produced at high angles of attack, but that is not an efficient region. Untwisted fin. Note that St and $C_{T,wing}$ ($=C_{X,wing}$ in the manuscript) during hovering are based on the induced velocity which are modeled assuming disk flow (Wakeling & Ellington 1997). The hovering data follow the trend of the tow data.

1.5 Quasi-steady modeling

Figures SI10 and 11 show detailed results of the modeling. The former shows the variations of forces and power when twist amplitudes are 0° (a), (b) 10° , (c) 20° , and (d) 40° . The latter shows similar information but at different spanwise panels.

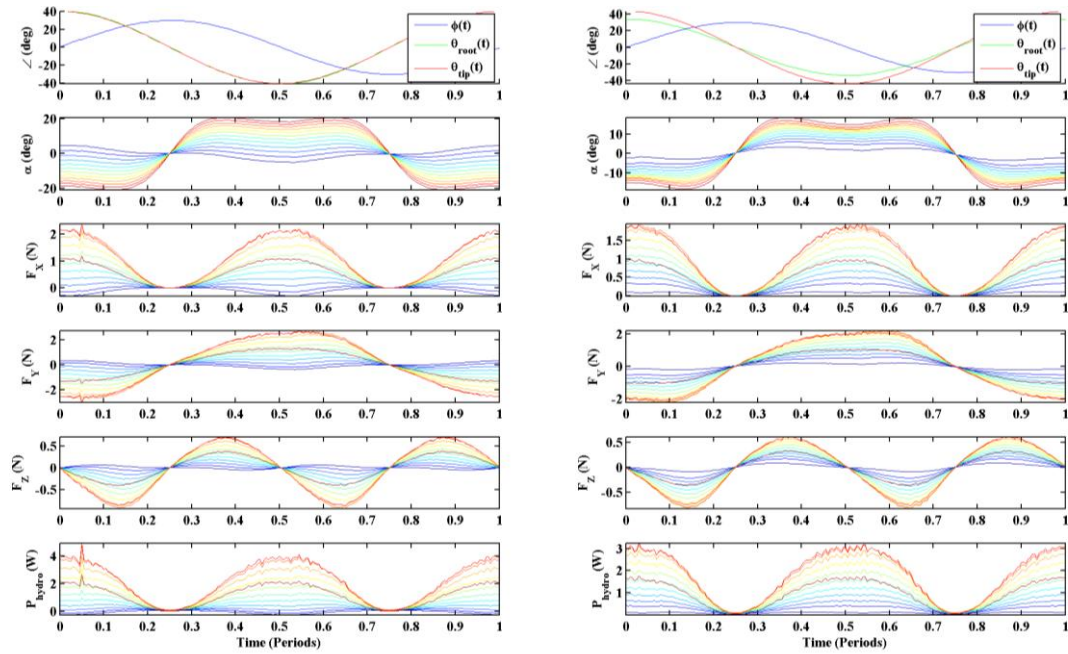




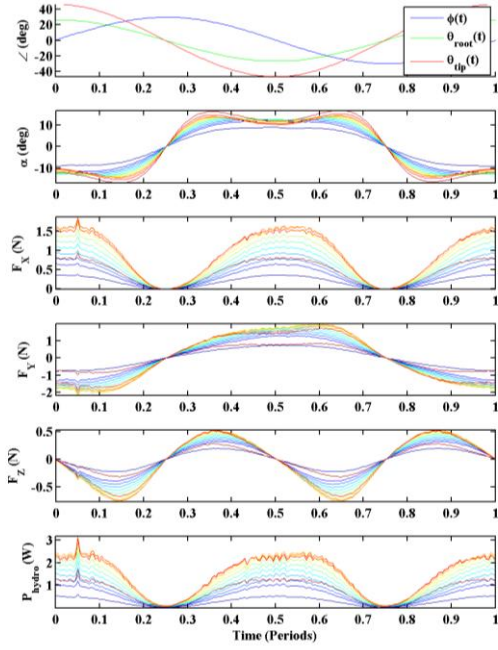
(c)

(d)

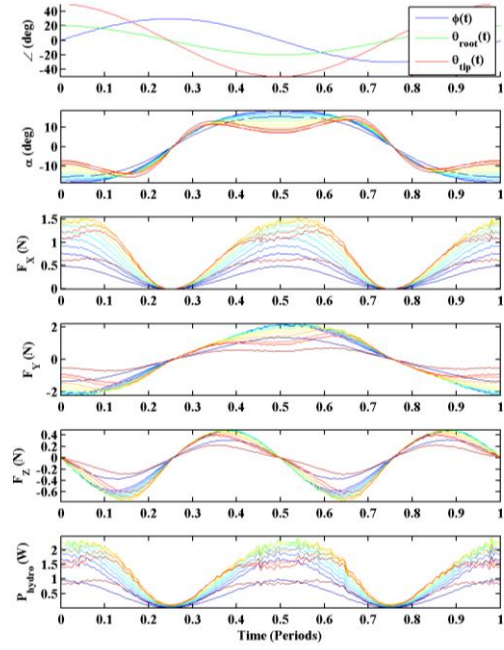
Figure SI10. Comparison of measurements and quasi-steady model at twist angles θ_{t0} of (a) 0° , (b) 10° , (c) 20° , and (d) 40° . The angles of attack are computed values. They are at panels along the span with color changing from blue at the root to red at the fin tip. Fin kinematics: $\phi_0 = 30^\circ$, $\theta_{R_{avg}} = 40^\circ$, $f = 1.00$ Hz, $U = 1.00$ m/s, $St = 0.41$.



(a) (b)



(c)



(d)

Figure SII1. Variation of the angle of attack, force coefficients, and power with twist, in panels along the span estimated using the cross-flow vortex model. Color: Root (blue), tip (red). Fin kinematics are: $\phi_0 = 30^\circ$, $\theta_{R_{avg}} = 40^\circ$, $f = 1.00$ Hz, $U = 1.00$ m/s, $St = 0.41$.

Twist angles θ_{t0} are: (a) 0° , (b) 10° , (c) 20° , and (d) 40° .

Part 2: Video

Video SI1: Disturbance rejection by flapping fin driven by van der Pol oscillator:

File Names:

(a) Fin Oscillator Roll vs Pitch Bandyopadhyay;

(b) van der Pol Disturbance Rejection xload yload traces Bandyopadhyay

Size and Format:

(a) 326 KB Windows Media™ Video File

(b) 2,467 KB with Audio Windows Media™ Video File

The fin is given a square pulse of external disturbance.

Reference: Bandyopadhyay et al. 2008b *IEEE Jou. Oceanic Engrg.*

Video SI2: Leading-Edge Vortex Dye Visualization in Rigid and Twisting Fins During Hovering:

File Name: LEV-Final.mov

Size: 8,638 KB

Format: Quick Time Movie